2009

Precession Electron Diffraction and its Advantages for Structural Fingerprinting in the Transmission Electron Microscope

Peter Moeck
Portland State University, pmoeck@pdx.edu

Sergei Rouvimov

Citation Details

Moeck, Peter, and Sergei Rouvimov. "Precession electron diffraction and its advantages for structural fingerprinting in the transmission electron microscope." Zeitschrift für Kristallographie International journal for structural, physical, and chemical aspects of crystalline materials 225, no. 2-3 (2010): 110-124.

Z. Kristallogr. **225** (2010) 110–124 / **DOI** 10.1524/zkri.2010.1162

Precession electron diffraction and its advantages for structural fingerprinting in the transmission electron microscope

Peter Moeck* and Sergei Rouvimov

Nano-Crystallography Group, Department of Physics, Portland State University and Oregon Nanoscience and Microtechnologies Institute, P.O. Box 751, Portland, OR 97207-0751, USA

Received January 15, 2009; accepted November 3, 2009

Precession electron diffraction / Structural fingerprinting

Abstract. The foundations of precession electron diffraction in a transmission electron microscope are outlined. A brief illustration of the fact that laboratory-based powder X-ray diffraction fingerprinting is not feasible for nanocrystals is given. A procedure for structural fingerprinting of nanocrystals on the basis of structural data that can be extracted from precession electron diffraction spot patterns is proposed.

Introduction

This paper outlines the foundations of precession electron diffraction (PED) in order to illustrate its utility for structural fingerprinting of nanocrystals in a transmission electron microscope (TEM). It complements our earlier studies [1–4], which had an experimental emphasis and were concerned with structural fingerprinting on the basis of the Fourier transform of high resolution transmission electron microscopy (HRTEM) images that were recorded in the weak phase-object approximation. Some of our experimental results with PED on silicon crystals will be shown. A brief discussion of powder X-ray fingerprinting and its limitations will also be given.

Since we published recently an extensive review of structural fingerprinting strategies in a TEM [5], there is no need to discuss (and reference) any of the "traditional" structural fingerprinting strategies in a TEM. "Traditional" refers here to strategies that combine information on the projected reciprocal lattice geometry with either spectroscopic information as routinely obtainable in an analytical TEM from the same crystalline sample area or prior knowledge on the chemical composition of the sample.

By contrast, the novelty of the strategy that will be illustrated here briefly is due to the combination of information on the projected reciprocal lattice geometry with information on the projected point symmetry, and approximate structure factor moduli [6–8]. This strategy is, however, only applicable to nanocrystals, since it relies on kinematic or quasi-kinematic scattering approximations. Quasi-kinematic means that the electron scattering is of an intermediate nature [9–14], which is dealt with by utilizing approximate correction factors to kinematic predictions.

Note that kinematic and quasi-kinematic approximations to the scattering of fast electrons do allow for the successful solving and refining of unknown crystal structures, see Ref. [15] for a recent review. That whole field is now known as "structural electron crystallography"[1] while its predecessor and parts of its theoretical foundation are commonly referred to as "electron diffraction structure analysis (EDSA)" [12–14]. Although with much more data processing, the solving and refining of unknown crystal structures is achieved on the basis of the same kind of experimental data that we propose to employ for structural fingerprinting.

In order to allow the reader to appreciate the limits that dynamical electron scattering effects set on the application of our structural fingerprinting strategy, a brief theory section on kinematic and quasi-kinematic approximations to the scattering of fast electrons will be given. Since there are simple relationships between structure factor moduli and diffracted intensities (and structure factor phases and the phases of the Fourier coefficients of the HRTEM image intensity distribution [5]) for kinematic diffraction conditions only, the standard procedure is to utilize quasi-kinematic approximations, when necessary, in order to correct the experimental data for dynamical electron scattering effects.

This approach is analogous to the one typically taken in structural electron crystallography and constitutes the *first pillar* of structural fingerprinting. Because model structures from a comprehensive database are the *second pillar* of structural fingerprinting and semi-quantitative structure factor information may suffice, the task is reduced to finding the one model structure that best fits a certain set of experimental data.

* Correspondence author (e-mail: pmoeck@pdx.edu)

[1] An analysis of the content of the 2006 edition of the Inorganic Crystal Structure Database by Thomas Weirich resulted in 522 structures that were solved and refined partially or completely by structural electron crystallography, http://www.gfe.rwth-aachen.de/sig4/index.htm.

The mainly inorganic subset [16] (with some 20,000 entries) of the Crystallography Open Database (COD) [17, 18] (with currently about 88,000 entries) needs to be mentioned here briefly because we plan to interface open-access search-match capabilities to this database. We already provide at our web server [19] visualizations of so called "lattice-fringe fingerprint plots", *i.e.*, one of the key concepts of our strategies that capture the projected reciprocal lattice geometry efficiently [5, 20]. Interactive visualizations of the three dimensional atomic arrangement [21] of the entries of these two open access databases are also provided at our web server [19] and one of our two local mirrors of the COD [18].

We will sketch out an opportunity to determine the shapes of nanocrystals from the shapes of partially integrated precession electron diffraction spots as recorded on high dynamic range media. The advantages that objective lens aberration corrected TEMs offer for precession electron diffraction will be briefly mentioned.

After having clarified its advantages, we will at the end of this paper quite confidently propose to utilize precession electron diffraction for structural fingerprinting of nanocrystals in the TEM. When compared to conventional (stationary primary electron beam) diffraction spot patterns, "superior", *i.e.* potentially more discriminatory, structural information at three hierarchical levels: (i) the projected reciprocal lattice geometry, (ii) the projected point symmetry, and (iii) estimates of structure factor moduli can be obtained from PED patterns. This information may frequently suffice for structural fingerprinting without additional spectroscopic information from the same nanocrystal or prior knowledge on its chemical composition as this is done traditionally, see Ref. [5] for a review.

Nanocrystals cannot be fingerprinted structurally by powder X-ray diffractometry

In powder X-ray diffraction fingerprinting, the three-dimensional (3D) crystal structure information is collapsed into a one-dimensional intensity profile plotted over the angles between the primary beam and the scattered beams. This ensures that the relative large abundance of structural 3D information can be utilized for the fingerprinting (at just one orientation of the sample in a diffractometer). The angular position and relative heights of Bragg peaks in X-ray diffractograms constitute the information that is principally employable for structural fingerprinting. Since there is no simple experimental test for the presence of textures in the crystalline powder when the popular Bragg-Brentano para-focussing diffractometer geometry is employed, the information on the relative peaks heights is often not utilized in structural fingerprinting. (Note that textures may result in significant deviations of the experimental Bragg peak heights from their counterparts in the database. Advanced structural fingerprinting strategies in powder X-ray diffractometry do, however, utilize fitting procedures to the whole pattern [22].)

While a "Hanawalt search" [23] employs the angular positions (reciprocal lattice vectors) of the three most intense X-ray powder diffraction peaks, a "Fink search" utilizes the eight (or ten) shortest reciprocal lattice vectors with reasonably high peak intensities. Utilizing either or both of these classical search strategies leads, usually together with some prior knowledge of chemical information, to an identification of an unknown by comparison with the entries of a comprehensive database such as the well known Powder Diffraction File [24].

The powder X-ray method works best for crystal sizes in the micrometer range, where kinematic X-ray diffraction on otherwise almost perfect crystal lattices results essentially in delta functions for the line profiles of the individual reflections. The convolution of these delta functions with the instrumental broadening function of a diffractometer determines the shape and width of the Bragg peaks in a powder X-ray diffractogram.

For smaller crystals, the situation becomes rather complex and the Bragg peaks may get simultaneously shifted as well as asymmetrically or even anisotropically broadened [25]. With reducing nanocrystal size, powder X-ray diffraction patterns become less and less characteristic because more and more Bragg peaks overlap due to their broadening [26]. As the Bragg peaks are broadening, their intensity also diminishes until they become difficult to distinguish from the background. Further complications arise from crystallite size and shape distributions in a nanocrystal ensemble [27]. All of these small crystallite size and morphology effects are detrimental to an unambiguous identification of a crystalline material from its powder X-ray diffractogram.

Nanocrystals may also possess surface and near surface regions that are highly distorted or relaxed with respect to the bulk crystal structure. Such distinct surface structures, in turn, result in X-ray powder diffraction patterns that are no longer characteristic of the crystalline bulk core [28]. Finally, certain technologically important materials, *e.g.*,

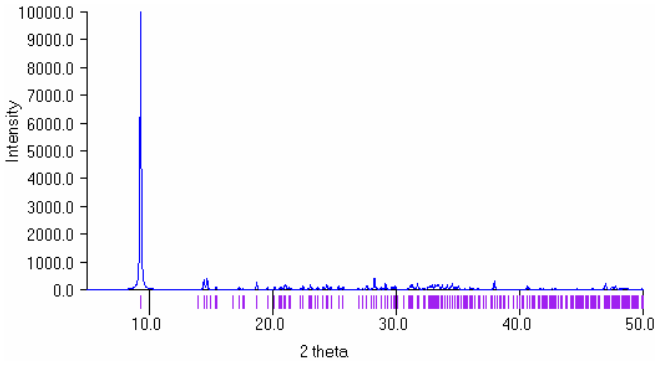

Fig. 1. Calculated X-ray powder diffractogram of vanadium-oxide nanotubes utilizing the characteristic K_α radiation from a Cu target. The theoretical positions of the Bragg peaks are marked at the abscissa. Because there is only one strong peak (with several higher order peaks), a classical Hanawalt search [23] would *not* work for the identification of this nanocrystalline material with tubular morphology. It is highly questionable if a Fink search would lead to an unambiguous identification either. In addition, it is known that the angular position of the strong (002) peak depends sensitively on the growth and processing conditions since protons (H^+) and/or small cations (Li^+) may become intercalated in this material. This powder diffraction pattern was simulated with the freeware program "Mercury", of the Cambridge Crystallographic Data Centre, downloadable at http://www.ccdc.cam.ac.uk/products/mercury/, using the structure data published in Ref. 29.

carbon nanotubes or vanadium-oxide nanotubes, do *not* give characteristic powder X-ray diffraction fingerprints by which the crystal structure can be identified out of a range of candidate structures from a comprehensive database, Fig. 1.

Such nanomaterials will, therefore, most likely not become part of general purpose X-ray powder diffraction databases. It is, therefore, fair to conclude that the otherwise very powerful powder X-ray diffraction technique becomes quite useless for crystal structure identifications in the nanometer size range.

Advantages of utilizing fast electrons for structural fingerprinting of nanocrystals

Nanometer crystal sizes have, on the other hand, exactly the opposite effect on the feasibility of our strategy of structural fingerprinting from PED patterns [5–7]. This is because as the crystal becomes smaller, its shape amplitude extends in reciprocal space. More diffraction spots will, therefore, appear in a PED pattern as intersections of diffracted electron beams (on a precessing Ewald sphere) with the plane recording medium of a TEM. The combined weak phase object/kinematic diffraction or phase object/quasi-kinematic diffraction approximations [7] of transmission electron microscopy (TEM) will also be reasonably well adhered to during the recording of the experimental data from nanometer sized crystallites.

The atomic scattering factors of the elements are for "fast" electrons about three orders of magnitudes larger than for X-rays. "Fast" refers here to some 50 to 80% of the speed of light, corresponding to electron wavelengths in the picometer range. This ensures that there will be sufficient diffracted intensity so that structural information is conveyed for fingerprinting purposes in the TEM even for the smallest of nanocrystals. On the other hand, this strong scattering of electrons by matter may complicate the analysis. The section on electron scattering approximations below will mention how dynamical diffraction effects can be taken into account and corrected for.

Kinematic and quasi-kinematic approximations to the scattering of fast electrons

The two-beam dynamical scattering theory (also known as the first Bethe approximation) suffices for many purposes. This approximation is an exact solution of the Schrödinger equation for the special case of only one strong diffracted beam in the diffraction pattern. As will be shown below, for vanishing crystal thickness (and short electron wavelengths, large unit cell volumes as well as small structure factor moduli), the predictions of the two-beam dynamical scattering theory closely approach the predictions of the kinematic theory.

The conceptual basis of the kinematic theory is single scattering of electrons by the electrostatic potential out of the primary beam into the diffracted beams while the former is negligibly attenuated. This is an idealized case for the scattering of fast electrons (while it typically suffices for the scattering of X-rays by crystals that are composed of mosaic blocks in the millimeter to centimeter range [9, 10]).

For nanometer sized crystals one can, however, reliably base crystallographic analyses by means of electron scattering on quasi-kinematic approximations and correct for primary extinction effects. (Note that the primary extinction correction is conceptually very similar to that employed in X-ray crystallography [9].)

The physical process of electron diffraction may be described mathematically by a Fourier transform. Electrons are scattered at the electrostatic potential energy distribution within the unit cell. This distribution peaks strongly at the positions of atoms. Following Ref. [9] and using some of its notation, the Fourier coefficients, Φ_{hkl}, of the electrostatic potential $\varphi(x, y, z)$ are given by the relation

$$\Phi_{hkl} = \int_{\Omega} \varphi(x, y, x) \cdot \exp\left\{2\pi i \left(h\,\frac{x}{a} + k\,\frac{y}{b} + l\,\frac{z}{c}\right)\right\} \mathrm{d}x\,\mathrm{d}y\,\mathrm{d}z\,, \tag{1}$$

where the dimension of Φ_{hkl} is volts times cube of length; $\Omega = \vec{a} \cdot (\vec{b} \times \vec{c})$ is the volume of the unit cell; $\vec{a}$, $\vec{b}$, $\vec{c}$ are the basis vectors, with *a, b, c* as their respective magnitudes; *h, k, l* are the Miller indices of the reflecting net plane; and *x, y, z* are the fractional coordinates of atoms in the unit cell. (Following the common practice of electron diffraction structure analysis, these Fourier coefficients are not normalized by the volume of the unit cell [9].)

These Fourier coefficients represent electron waves that are scattered by the electrostatic potential of the crystal in directions that are defined by Bragg's law ($\lambda = 2d_{HKL} \cdot \sin\Theta$, with Θ as half of the angle between the transmitted and scattered electron beams) and recorded a large distance away from the crystal.

The structure factor, F_{hkl}, with dimension of length is in case of electron scattering given by

$$F_{hkl} = \frac{\sigma}{\lambda}\,\Phi_{hkl}\,, \tag{2}$$

where $\sigma = \dfrac{2\pi \cdot m \cdot e \cdot \lambda}{h^2}$ is the "interaction parameter" with m as (relativistic) mass of the electron, e as elemental charge (*i.e.* modulus of the electronic charge), λ as (relativistic) electron wavelength, and h as Planck's constant.

In the first Born approximation (to the solution of the Schrödinger equation for the scattering of an electron by the electrostatic potential of an atom), *i.e.* in the kinematic electron scattering theory, the structure factors are given by the relation

$$F_{hkl} = \sum_j f_j \cdot f_T^j \cdot \exp 2\pi i(hx_j + ky_j + lz_j)\,, \tag{3}$$

where f_j are the atomic scattering factor for electrons, and f^j_T are the respective temperature factors for all j atoms in the unit cell. Note that temperature factors are much less important for electrons than for X-rays. This is because the atomic scattering factors for electrons fall off with $(\sin\Theta/\lambda)^2$, *i.e.* much more rapidly than their counterparts for X-rays. While the first Born approximation ensures

that the atomic scattering factors are real numbers, the structure factors are complex numbers with a modulus and phase (angle).

For an *ideal* single (parallelepiped shaped) crystal, the two-beam dynamical diffraction theory predicts for the intensity of a diffracted beam, (*i.e.* of a reflection in an electron diffraction spot pattern):

$$I_{hkl} = I_0 S \cdot Q^2 \, \frac{\sin^2 \{A \cdot [(\pi H)^2 + Q^2]^{0.5}\}}{(\pi H)^2 + Q^2} \tag{4}$$

where I_0 is the intensity of the primary electron beam; S is the area of the crystal that is illuminated by the primary electron beam; $Q = \lambda/\Omega \cdot |F_{hkl}| = \sigma/\Omega \cdot |\Phi_{hkl}|$ is an entity that is proportional to a particular structure factor modulus (and Fourier coefficient modulus of the electrostatic potential); A is the crystal thickness; and H is the extension of the reflection in reciprocal space (measured from the exact reciprocal lattice point position parallel to the primary electron beam direction). For comparison with treatments by other authors, note that $Q = \pi \cdot \cos \Theta/\xi_{hkl}$, where ξ_{hkl} is known as "extinction distance".)

The respective prediction of the kinematic theory for an *ideal* single (parallelepiped shaped) crystal is:

$$I_{hkl} = I_0 S \cdot Q^2 \, \frac{\sin^2 \{A \cdot \pi H\}}{(\pi H)^2} \, . \tag{5}$$

When Q is much smaller than πH, relation (4) can be approximated by relation (5). Because H is inversely proportional to the thickness of the crystal, it becomes larger as the nanocrystal gets thinner. In other words, for sufficiently thin crystals, the two-beam dynamical diffraction theory is well approximated by the kinematic theory. For $H = 0$ relation (4) becomes

$$I_{hkl}^{\mathrm{MAX}} = I_0 S \cdot \sin^2(Q \cdot A) \tag{6a}$$

and relation (5) becomes

$$I_{hkl}^{\mathrm{MAX}} = I_0 S \cdot (Q \cdot A)^2 \, . \tag{6b}$$

The square of the sine function in (6a) may be replaced by the square of the argument for small $Q \cdot A$, so that relation (6b) becomes a good approximation to the former relation. Note that the nature of the electron scattering phenomena is revealed in relations (4) to (6b), but one does not base structural electron crystallography or structural fingerprinting strategies that employ structure factor information directly on them. For that these theoretical relations need to be modified by Lorentz factors that refer to the prevailing experimental conditions.

The ratio of the integrated scattered beam intensity to the initial beam intensity received by a *real* crystalline sample from the primary beam in a *real* electron scattering experiment is referred to as "integrated coefficient of reflection" [9]. It is in the kinematic theory given by the relation

$$\frac{I_{hkl}}{I_0 S} = Q^2 \cdot A \cdot L \, , \tag{7}$$

where L is a Lorentz factor and possesses the unit of length. Analogously to their counterparts in X-ray diffraction, Lorentz factors account for the physical particulars (including the relative time intervals) of the intersections of the Ewald sphere with the shape amplitude of the nanocrystals around the accessible reciprocal lattice points.

The nature of the Lorentz factor differs from experimental set up to experiment set up, *i.e.* with both the diffraction technique and the crystalline sample type. Within a certain diffraction technique and crystalline sample type, the Lorentz factor varies only quantitatively [9, 10]. For now it may suffice that making L smaller than A and/or Q^{-1} by choice of certain parameters of a diffraction technique or by choice of the selection of a certain crystalline sample reduces the integrated coefficient of reflection so that structural fingerprinting may proceed within the frameworks of kinematic or quasi-kinematic electron scattering theories.

Since a particular Q is proportional to a particular structure factor modulus, which is a parameter of a crystal structure, relation (5) will for different reflections *(hkl)* of the same nanocrystal with a fixed size be a better or worse approximation to relation (4). The electron wavelength, size/thickness and structure of the nanocrystal, as well as the volume of its unit cell are fixed in a typical experiment, but are also parameters that determine how well the two-beam dynamical diffraction theory will be approximated by the kinematic theory.

It is, therefore, helpful to introduce a "range of crystal sizes/thicknesses, structure factor moduli, electron wavelengths, and unit cell volumes" in which a nanocrystal diffracts quasi-kinematically. In general, the "electron scattering centers" (*i.e.* atoms and ions) with higher atomic number possess for the same scattering angle higher scattering factors than their lower atomic number counterparts. The mutual arrangement of the "electron scattering centers" determines the electrostatic potential. While for face-centered cubic structures of elements such as aluminum all atoms scatter in phase, *i.e.* their individual contributions to the scattered waves add up, there will be constructive and destructive interference in more complex structures. Also, there are typically more reflections for structures with large unit cell volumes than there are for structures with small unit cell volumes. In addition, the reflections from large unit cells tend to be weaker than their counterparts from structures with small unit cells. The crystal orientation determines through Bragg's law which reflections will be activated in a given experiment and, therefore, affects indirectly the "range" in which a nanocrystal diffracts quasi-kinematically.

Since no definitive crystal size/thickness limit for the "quasi-kinematic diffraction range" can be given that would apply to all nanocrystals and all experiments, one may employ the relation

$$Q \cdot A' = \frac{\lambda}{\Omega} \cdot |F_{hkl}| \cdot A' = \frac{\sigma}{\vec{a} \cdot (\vec{b} \times \vec{c})} \cdot |\Phi_{hkl}| \cdot A' \leq 1 \approx 1 \, , \tag{8}$$

where A' has the meaning of Vainshtein's "critical thickness range" [9–13], as an evaluation criterion for the gradual transition from the kinematic theory to the dynamical two-beam theory. (Note that a relation analogous to Eq. (8) applies to X-ray scattering as well and there are also

relations analogous to those given further above for the kinematic and two-beam dynamical scattering theories of X-rays [10].) Individual reflections of the same nanocrystal, *i.e.* for a fixed A, λ and Ω may well behave differently. The reflections that possess small structure factor moduli may behave nearly kinetically and the ones with intermediate and large structure factor moduli may behave quasi-kinematically.

As first proposed by Blackman [30], corrections for primary extinction effects can be made in the two-beam approximation as long as the experimental diffraction technique provides an effective integration of the reflection intensities [9, 31, 32]. For precession electron diffraction experiments with large precession angles, such integration is reasonably well achieved for inorganic crystals that are no more than a few tens of nanometer thick. For small precession angles, on the other hand, one will obtain at least a partial integration of the reflection intensities.

In addition, one may deal with systematic n-beam interactions of selected systematic rows, *e.g.* for (*h00*), (*hh0*), and (*hhh*) reflections that are higher orders ($n = 2, 3, \ldots$) of strong reflections with $h = 1$ or 2, by means of the second Bethe approximation, the so called "Bethe dynamic potentials" [32–34]. As in the Blackman correction, no prior knowledge of either the crystal thickness or orientation is needed for the application of this correction [33].

The phase grating approximation to dynamical multiple beam scattering can also be used to extract quasi-kinematic structure factors from electron diffraction intensities on the basis of two experimental datasets that were recorded for the same kind of crystallites at a highest voltage TEM (*e.g.* 1,000 kV) and an intermediated voltage (or 100 kV) TEM [35]. This approach is highly advantageous as the reflections which need to be corrected can be identified directly.

Opportunity of determining nanocrystal shapes from the shapes of partially integrated precession electron diffraction spots

As clearly stated above, relations (4) and (5) are only valid for a thin parallelepiped shaped crystal. While the dimension of the crystal is assumed to be very small in the direction of the transmitted primary electron beam (*i.e.* its thickness, A, is supposed to be in the nanometer to tens of nanometers range in other words), the remaining two dimensions of the "platelet" are considered to be very large. Other crystal shapes, especially those of nanocrystals where all three dimensions are very small, require, therefore, modifications to relations (4) and (5). The main conclusions of the previous section, *i.e.* that the kinematical theory is a small $Q \cdot A$ approximation to the two-beam dynamical theory and that there is some critical thickness range remain, however, valid for nanocrystals of other shapes as well.

The concepts of a direct space shape function (which is unity inside the crystal and zero everywhere else) and its Fourier transform, the shape amplitude function, can be employed to deal with crystal shape effects on the distribution of diffracted intensities in reciprocal space [36–39]. The 3D crystal form factor is the shape amplitude function multiplied by its complex conjugate function. Two dimensional (2D) sections through it are in principle observable experimentally in an electron diffraction experiment if the crystal is sufficiently small [9].

Expanding on relations (4) and (5) for ideal (thin parallelepiped shaped) crystals, Ref. [9] notes that the attenuating subsidiary maxima of the Fourier transform of the shape function in the direction of the primary electron beam is given by the relation

$$H(n) = \left[\left(\frac{n}{2A}\right)^2 - \left(\frac{Q^2}{\pi^2}\right)\right]^{0.5} . \tag{9a}$$

The n is an integer that is even (and larger than two) for all zero values of relation (4) that separate the central interference maximum and all attenuating subsidiary maxima of a diffracted beam. The respective prediction of the kinematic theory is

$$H(n) = \frac{n}{2A} . \tag{9b}$$

The term $-Q^2/\pi^2$ under the square root in relation (9a) is not significant when the crystal thickness A is small, *i.e.* when the kinematical approximation is applicable, and when the values of n are low. Under these conditions, relation (9b) approximates relation (9a) well. This means that within the quasi-kinematic thickness range, the subsidiary intensity maxima of a reflection will be at about the same place in reciprocal space.

This is approximately true for other crystal shapes as well and gives a justification to calculate shape amplitude functions and crystal form factors of nanocrystals in the kinematic approximation. In addition, there is experimental evidence for this [37] when the nanocrystals are less than about 50 to 100 nm, do not contain heavy atoms (such as, *e.g.*, Pb or Au), and possess crystal structures where not all atoms scatter in phase (such as, *e.g.*, $Fm\bar{3}m$).

The shape amplitude function and the crystal form factor are the same for all kinematically allowed reflection in an electron diffraction experiment. Due to the curvature of the Ewald sphere, different sections through the 3D crystal form factor will be observed in a conventional (stationary primary electron beam) diffraction experiment as different 2D shapes of the reflections.

While the general formulae to calculate "crystal form factor maps" for any kind of crystalline polyhedron are given in Refs. [36, 37], their specific counterparts for the five platonic polyhedra (including the two that are possible shapes of single-domain quasi-crystals) are given in Refs. [38, 39]. Such maps can be directly compared to the experimentally obtained (2D) reflection shape in order to estimate the (3D) shape of a small crystal [37].

Since precession electron diffraction involves a "precessing Ewald sphere" where reflections further out in reciprocal space may be better integrated, there should be additional systematic changes in the experimentally obtainable 2D shapes of the reflections (as recorded on a flat recording medium with a high dynamical range) whenever there is partial integration over the excitation error. (The 3D crystal form factor of all reflections will remain to be

the same for all reflections. In case of complete integration of all reflections, there can only be minor changes in the experimentally obtainable total 2D intensity (but not its distribution) as different reflections spend slightly different amounts of time in reflection position).

Both the variation in the 2D shape of the reflections due to the curvature of the Ewald sphere and systematic changes due to their incomplete integration by its precession movement could possibly be utilized to derive and estimate the actual shape of a diffracting nanocrystal in a TEM with precession add-on instrumentaiton[2] by reference to corresponding simulations along the lines of Refs. [36–39]. Such analyses will become more important in the future as crystallographic nano-materials-science and -engineering progresses, because "unconventional" crystallite shapes have been linked to enhanced catalytic activity, *e.g.* Ref. [40].

Improvements in the focalization of the primary electron beam on the sample during precession over what can be obtained with current precession diffraction add-on instrumentation[2] may, however, be necessary to perform such analyses experimentally. Also the exploitation of this opportunity may require the correction of major electron-optical aberrations of the objective lens. Since precession electron diffraction suppresses dynamical diffraction effects for sufficiently small nanocrystals (to be discussed in more detail below), it better justifies the calculation of crystal form factor maps in the kinematic approximation [36–39]. As a result of this, there may still be a net benefit of utilizing PED for the determination of the 3D shape of nanocrystals.

Precession electron diffraction patterns of individual nanocrystals

The precession electron diffraction (PED) method, also referred to as Vincent-Midgley technique due to the seminal paper [41] of these authors, is formally analogous to the well known X-ray (Buerger) precession technique [42]. It utilizes, however, a precession movement of the primary electron beam around the microscope's optical axis rather than that of a single crystal around a fixed primary X-ray beam direction. Due to the much larger radius of the Ewald sphere, the equivalents of "layer line screens" [42] are not used for fast electrons. For essentially the same reason and in order to avoid uncontrolled excitation of reflections from higher order Laue zones, the precession angles are an order of magnitude smaller in the case of precession electron diffraction. The primary electron beam can be either parallel or slightly convergent and its precession creates a hollow illumination cone which has its vertex on the crystalline sample.

The primary electron beam and the diffracted beams are de-scanned (after they have left the nanocrystal) in such a manner that stationary[2] diffraction patterns are obtained on the (stationary) viewing screen of the TEM or the recoding medium underneath this screen. (Note that in the Buerger precession technique, the plane recording film is precessed synchronously with the crystal. This synchronous precession movement is a requirement of the generalization of the de Jong-Bouman principle and leads to an undistorted recording of the reciprocal lattice [42].)

[2] Electron precession add-on devices to older and newer mid-voltage TEMs have been commercialized under the name "Spinning Star" by Stavros Nicolopoulos and coworkers at the company NanoMEGAS SPRL; http://www.nanomegas.com; (Avilov, A. S.; Kuligin, K. V.; Nicolopoulos, S.: A method for measuring diffraction patterns from a transmission electron microscopy to determine crystal structures and a device therefor, WO/2005/022582, PCT/EP2003/009727, international filing date 02/09/2003). The formation of a "precession electron diffraction community" that comprises currently about 40 researchers and groups worldwide resulted from the creation of these devices.

A digital, second generation "Spinning Star" is at the core of the ASTAR system [78] of the NanoMEGAS company. This precession electron diffraction device is frequently referred to as "DigiStar" and allows in combination with an external digital camera for fast and highly reliable "crystal orientations & phases" map acquisitions with any older or newer mid-voltage TEM. The ASTAR system is superior to the complementary electron backscatter diffraction technique (EBSD) in scanning electron microscopy (SEM), because it is based on precessed transmission spot-diffraction patterns rather than "near-surface backscattered" Kikuchi diffraction patterns. The former patterns are much less sensitive to the plastic deformation state of the crystals and their real structure content than Kikuchi patterns. In addition, the orientations and crystal structures of smaller crystallites can be mapped in a TEM due to the transmission geometry and higher acceleration voltages.

The software control of the "DigiStar" allows for a better focalization of the primary electron beam onto the sample during the precession movement. A six times smaller precessing primary electron beam diameter has, for example, been observed as resulting from the optimization of the software control of a "DigiStar" alone when all other electron optical settings on the TEM remained unaltered (Stavros Nicolopoulos, private communication).

Portland State University's "Laboratory for Structural Fingerprinting and Electron Crystallography" (which is run by the first author of this paper) serves as the first demonstration site for the NanoMEGAS company in the Americas. A "DigiStar" is interfaced there to an analytical FEI Tecnai G^2 F20 ST field-emission gun TEM and can be demonstrated on request. A first generation (analog) precession diffraction device "Spinning Star" is interfaced at Portland State University's "Materials and Manufacturing Research Institute" to an analytical JEOL JEM 2000FX (with LaB_6 gun) and can also be demonstrated on request (to the first author of this paper). The whole suite of electron crystallography software from Calidris and AnaliTEX (see footnote 3) can be demonstrated at the "Laboratory for Structural Fingerprinting and Electron Crystallography" as well.

Laurence D. Mark's group at Northwestern University created over recent years three types of precession electron diffraction add-on devices to mid-voltage TEMs (Own, C. S., Marks, L. D.; Sinkler, W.: Electron precession: A guide for implementation. Rev. Sci. Instrum. **76** (2005) 033703; Own, C. S., Marks, L. D.: Hollow-cone electron diffraction system. US Patent application no: 60/531,641, December 2004). Copies of such devices have been installed at the Frederick Seitz Materials Research Laboratory of the University of Illinois at Urbana-Champaign, Northwestern University, Arizona State University, and UOP LLC (formerly known as Universal Oil Products at Des Plaines). For the last two years, Christopher Su-Yan Own's company Ack! INDUSTRIES has offered digital electron precession diffraction add-on instrumentation (see, *e.g.*, http://csown.dhs.org/papers/PrecManual1.0.pdf) as well.

The latest precession electron diffraction device of Laurence D. Mark's group (Ciston, J.; Deng, B.; Marks, L. D.; Sinkler, W.; Own, C. S.: Precession electron diffraction: Optimized experimental conditions to detect valence charge density. Micros. Microanal. **13**, Suppl. 2, (2007) 950CD-951CD) enables arbitrary (non-circular) waveforms so that the excitation of systematic row conditions can be avoided. As illustrated by the list of references, this group is also a leader in most other developments around precession electron diffraction.

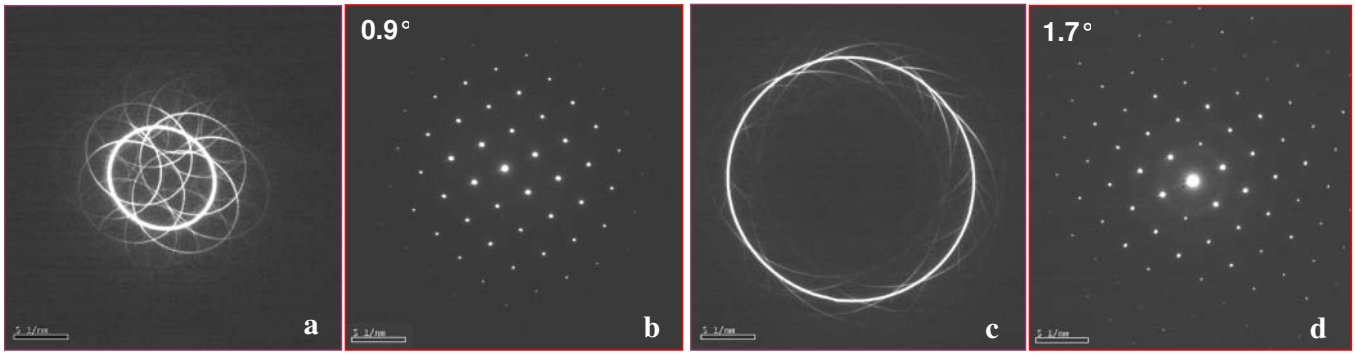

Fig. 2. Experimental PED patterns of a silicon crystal close to the [110] zone axis and with 40 nm approximate thickness. **(a)** and **(c)** "just-precessed" mode; **(b)** and **(d)** "properly de-scanned" mode so that stationary spot diffraction patterns results. Precession angles of either 0.9° (a) and (b) or 1.7° (c) and (d) were utilized.

The advantages of a precessing primary electron beam for structural electron crystallography in both the diffraction and high resolution imaging modes of TEMs were already realized in the mid 1970s of the last century, *e.g.* Ref. [43]. Many older TEMs do allow for an "electronic" hollow cone illumination with small semi-cone angles [44] but not for a "proper descaning", which is the hallmark of the commercially available precession electron diffraction add-ons to (older and newer) mid-voltage TEMs[2].

Figure 2 shows experimental PED patterns from a silicon crystal in both the "just-precessed" and "properly de-scanned" modes. In the latter mode, Fig. 2b and d, all of the fine arcs and circles of intensity of Fig. 2a and c are "integrated" into sharp diffraction spots. The strongest circles in Fig. 2a and c are due to the primary electron beam and its proper de-scanning results in the central 000 spot in the PED patterns of Fig. 2b and d.

All of the following experimental PED patterns will be shown only in the properly de-scanned mode and were recorded from silicon crystals close to the [110] orientation with electrons that had been accelerated by a potential of 200 kV. The respective thicknesses of the wedge shaped crystals were in each case derived from clearly visible thickness fringes.

Figure 3 shows sketches that illustrate the effect of a precessing primary electron beam on the [110] zone-axis diffraction pattern of a silicon nanocrystal. The precession movement of the primary electron beam around the center

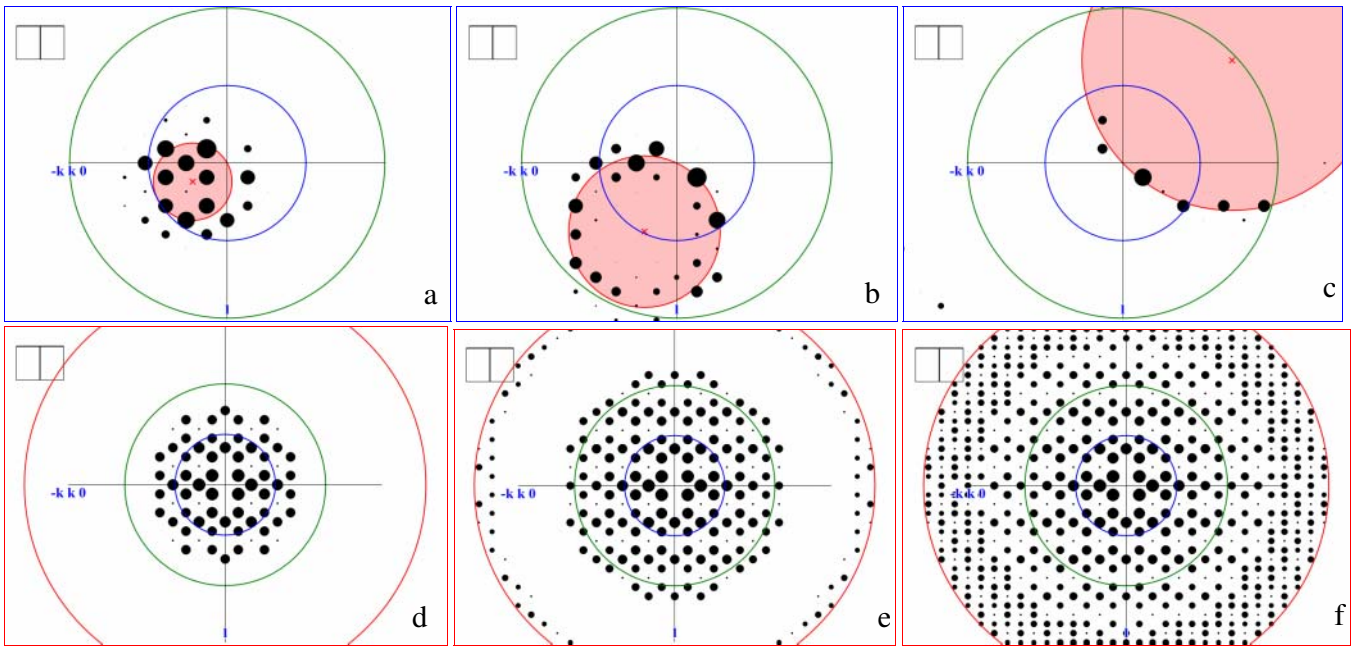

Fig. 3. Sketches of PED patterns for silicon, [110] zone axis, 200 kV, 10 nm thickness, calculated under kinematic assumptions. The weak spots represent kinematically forbidden *hkl* reflections, where all indices are even, neither of them is zero, and their sum is not a modulus of 4. The other reflections are drawn with a spot size that is proportional to the structure factor, $\sim F_{hkl}$. While the two concentric rings in the top row represent 0.05 nm (or 20 nm^{-1}, outer ring), and 0.1 nm (or 10 nm^{-1}, inner ring), their three counterparts in the bottom row represent 0.025 nm (or 40 nm^{-1}), 0.05 nm, and 0.1 nm, respectively. The three columns are for precession angles of 0.72, 1.4, and 2.8, respectively. **(a–c)** Snap shots of the formation of PED patterns. The shaded circle represents the (otherwise rotating) Laue circle. **(d–f)** Sketches of stationary PED patterns. Note the presence of reflections from the second order Laue zone in (c), (e), and (f) as well as other effects of an increasing precession angle (from left to right) in both rows. The program "eMap" (version 1.2, 2008) of the AnaliTEX company has been used to create these sketches (and the two rectangular boxes in each of the figures represent a cube viewed along the [110] direction).

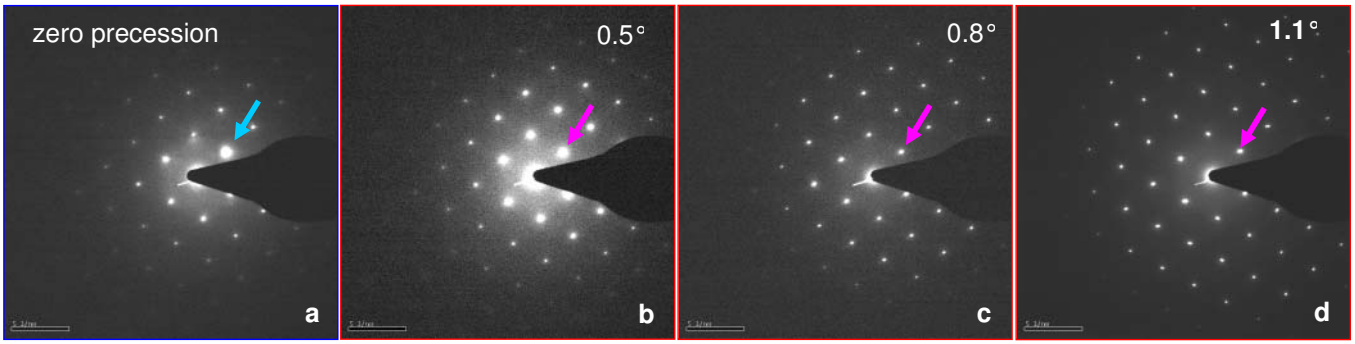

Fig. 4. Experimental diffraction patterns from a crushed (wedge shaped) silicon crystal. The thickness was approximately 60 nm and the crystal orientation was close to the [110] zone axis. **(a)** SAED pattern (zero precession), **(b)**, **(c)** and **(d)** PED patterns from the same sample area with increasing precession angle. Note that while the intensity of the $(1\bar{1}\bar{1})$ reflection, marked by an arrow in each diffraction pattern, is much higher than that of its Friedel pair $(\bar{1}11)$ and that of the other two symmetry equivalent $\pm(1\bar{1}1)$ reflections in the SAED pattern (a), the intensities of all four symmetry equivalent {111} reflections are very similar for the PED patterns (b–d).

of the viewing screen of the TEM, Fig. 2a and c, in direct space can be visualized in reciprocal space by the rotation of the so called "Laue circle", Fig. 3a–c around the central *000* spot in the (stationary) diffraction patterns of Fig. 2b and 2. The radius of the Laue circle is determined by the precession angle, *i.e.* the half angle of the hollow illumination cone of the precessing primary electron beam. (The precession angle can be calibrated on the basis of the radius of the primary electron beam circle in "just-precessed" mode recordings such as Fig. 2a and c.)

The Ewald sphere will be intersected sequentially at positions that are close to the circumference of the Laue circles, Fig. 3a–c. Note that individual reflections and rows of reflections of silicon are excited sequentially (as much as this is possible with current technology in a TEM[2]). This sequential excitement of reflections and rows of reflections reduces the number of viable multiple diffraction scattering paths between different reflections and rows of reflections at any one time. It, thus, reduces non-systematic multiple scattering effects significantly. Systematic dynamical scattering within a systematic row are, on the other hand, not suppressed by the precession movement [41].

A comparison of the conventional (zero precession, stationary primary electron beam) selected area electron diffraction (SAED) pattern, Fig. 4a, with its PED pattern counterparts, Fig. 4b–d, demonstrates that a nanocrystal does not need to be oriented with a low indexed zone-axis exactly parallel to the optical axis of the TEM in order to allow for advanced structural fingerprinting in the TEM on the basis of the diffracted intensities [6, 7].

Utilizing the program "Space Group Determinator" in conjunction with "CRISP/ELD" from the Calidris company[3], a quantification of the Friedel pair symmetry in this series of diffraction patterns gives the "intensity residuals"[4] 48.3% for Fig. 4a, 36.1% for Fig. 4b, 30.8% for Fig. 4c, and 21% for Fig. 4d. (Note that an ideal Friedel pair symmetry would result in an intensity residual of 0%, but cannot be obtained experimentally due to asymmetric single and/or multiple electron scattering whenever the slightest crystal mis-orientation, beam tilt mis-alignment, or crystal thickness variation exists. In addition, current precession add-on instrumentation[2] utilizes precession movements of the primary electron beam around a full 360° cycle, so that each reflection is twice in reflection condition. If the primary electron beam is not optimally focused on the crystal, this may lead to the appearance of two Bragg spots instead of just one perfectly superimposed spot.)

As shown in Fig. 5a, the primary electron beam may be slightly tilted with respect to the optical axis of the TEM. The comparison of the SAED pattern, Fig. 5a, with its PED counterpart patterns, Fig. 5b and c, illustrates, however, that structural fingerprinting from PED patterns will not be affected unduly by such primary electron beam tilt mis-alignments. These tolerances to crystal mis-orientations and primary electron beam tilt mis-alignments lessen the experimental efforts for effective structural fingerprinting on the basis of PED patterns [6, 7].

Compared to the SAED patterns from the respective three silicon crystals, Figs. 4a, 5a, and 6a, there are frequently many more reflections in the PED patterns, Figs. 4b–d, 5b, c, 6b and c, from nanocrystals with low defect content[5] such as silicon. This is especially true for higher

[3] The programs "CRISP/ELD" and "Space Group Determinator" run on IBM compatible personal computers. These programs are part of a comprehensive software suite for structural electron crystallography, have been developed by Xiaodong Zou, Sven Hovmöller, and coworkers, and can be ordered at http://www.calidris-em.com. The program "eMap" by Peter Oleynikov (AnaliTEX) complements this software suite (runs also on IBM compatible personal computers) and can also be ordered over the Calidris website.

[4] The intensity residual of Friedel pairs in an electron diffraction pattern is defined by the relation

$$I_{RES} = \frac{\sum_{H,K} |I(H,K) - \frac{1}{2}\{I(H,K) + I(-H,-K)\}|}{\sum_{H,K} I(H,K)},$$

where H and K are 2D reciprocal lattice coordinates of electron diffraction spots.

[5] For nanocrystals of "low crystalline perfection", *e.g.* various zeolites, it was observed by us and Stavros Nicolopoulos that the number of reflections in a precession electron diffraction pattern may decrease with increasing precession angle. This can be explained straightforwardly by a reduction of "defect mediated" secondary scattering (see Ref. [31] or Cowley, J. M.; Rees, A. L.; Spink, J. A.:

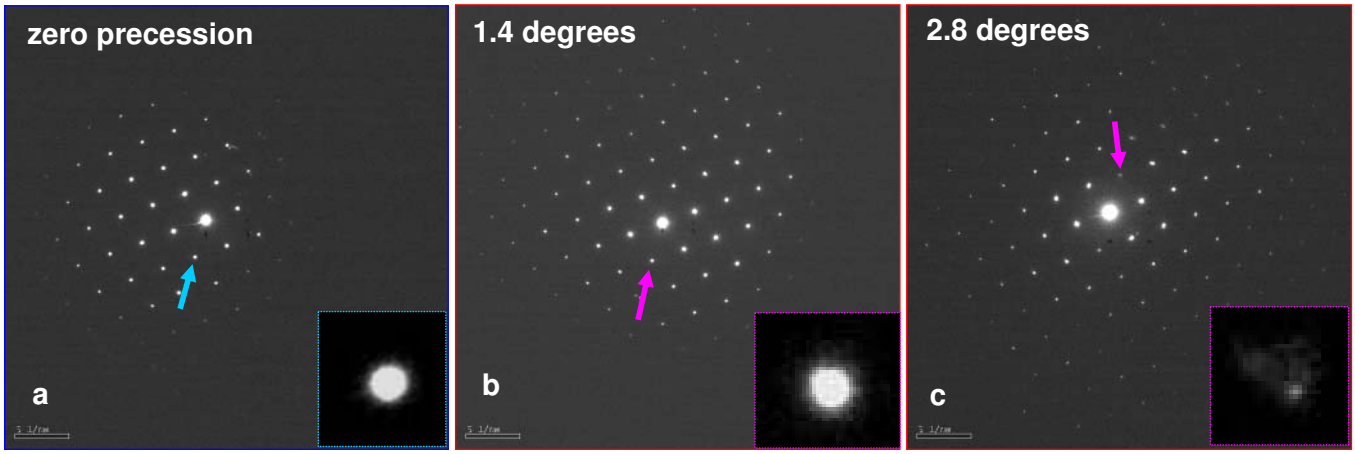

Fig. 5. Experimental diffraction patterns close to the [110] zone axis (200 kV) from a thicker part of a wedged shaped silicon crystal that was prepared in a focused ion beam microscope. The thickness was approximately 56 nm. **(a)** SAED pattern (zero precession). Note the slight mis-alignment of the primary electron beam in (a). **(b)** and **(c)** PED patterns (with the same primary electron beam-tilt mis-alignment with respect to the optical axis of the TEM) from the same sample area with increasing precession angle. One member of the kinematically forbidden (002) reflections is marked by an arrow in each diffraction pattern and also shown magnified in the insets.

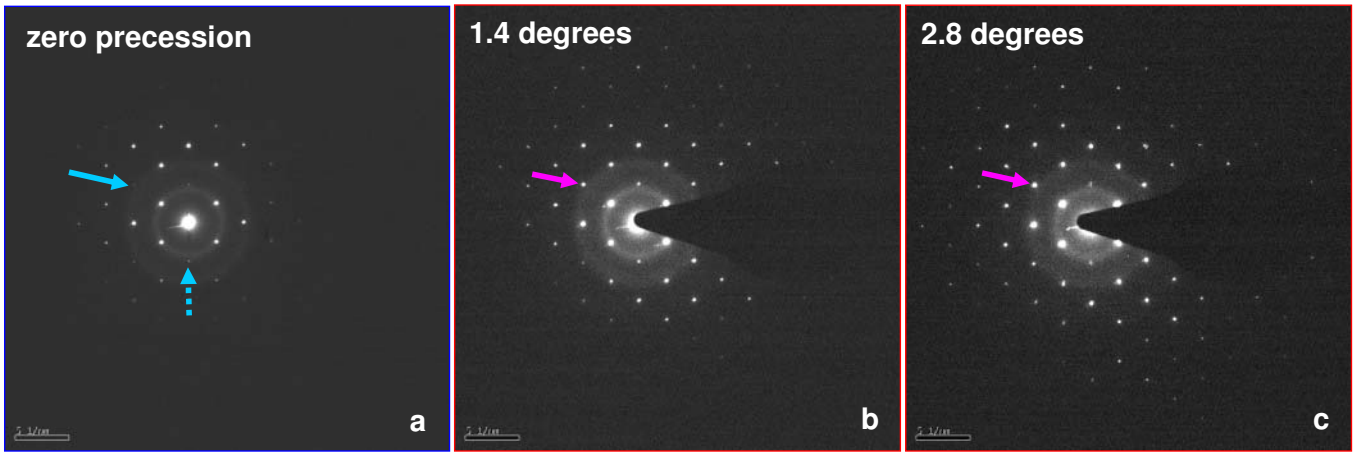

Fig. 6. Experimental diffraction patterns close to the [110] zone axis (200 kV) from the thinnest part of a wedge shaped silicon crystal that was prepared in a focused ion-beam microscope. The thickness was approximately 6 nm. **(a)** SAED pattern (zero precession). **(b)** and **(c)** PED patterns from the same sample area with increasing precession angle. All diffraction patterns were recorded close to the amorphized edge region of the sample that borders on the vacuum region within the electron microscope. This explains the relatively strong asymmetry of the SAED pattern (a) with respect to its center. The concentric rings of intensity in all diffraction patterns arise from the above mentioned amorphized edge region. While the kinematically forbidden $(00\bar{2})$ reflection is marked by a dotted arrow in (a) only, the kinematically forbidden $(2\bar{2}2)$ reflection is marked by a full arrow in each diffraction pattern.

precession angles. More reflections allow for least-squares fits to larger systems of inhomogeneous linear equations [6, 7]. This results in more precise determinations of projected reciprocal lattice geometries. The initial projected reciprocal lattice geometry based identification step of structural fingerprinting in the TEM [6, 7] can, therefore, be improved on the basis of PED patterns.

Most important for advanced structural fingerprinting purposes in the TEM [6, 7], single-crystal PED patterns deliver frequently (at least partially) integrated diffraction spot intensities that can be treated as either kinematical or quasi-kinematical for crystals that are up to several tens of nanometers thick. By no means does this imply that the electron diffraction reflection intensities are indeed of a kinematical nature. This only means that quasi-kinematical corrections for two-beam and systematic row interactions effects to experimental electron reflection intensities [30–34] suffice frequently within this thickness range for inorganic crystals [15, 34, 41, 45–88]. Often these corrections are not even necessary.

When the dynamical diffraction effects are weak, they may be ignored altogether and the experimental reflection intensities data may be utilized for the extraction of the squares of the structure factor moduli without dynamical corrections. This will be the case for sufficiently thin crystallites. Complimentarily for thick crystallites, the data may be treated as adhering to the asymptotic limit of the two-beam diffraction model [30] and the first power of the structure factor moduli may be extracted from the experimental reflection intensities. For intermediate crystallite

Secondary Elastic Scattering in Electron Diffraction. Proc. Phys. Soc. A**64** (1951) 609–619). Crystallites that are too thick for structural electron crystallography or advanced structural fingerprinting in the TEM may show a similar tendency.

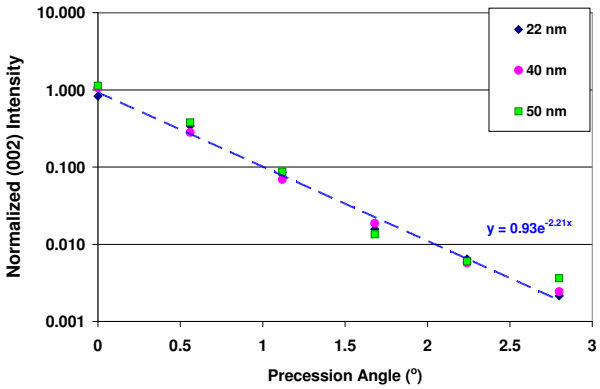

Fig. 7. Effect of the precession angle on the "normalized peak" intensities of the kinematically forbidden ±(002) reflections in the [110] zone axis orientation for three silicon crystallites with thicknesses in the range of 22 to 50 nm. The peak intensities were averaged over both members of this Friedel pair. The normalization was performed by dividing the maximal peak intensity of the reflections by the maximal peak intensity of the primary electron beam. (The data were recorded at 200 kV in the nano-beam mode).

thicknesses, a simple two-beam primary extinction correction may be sufficient [9]. These more general statements will now be followed by specific discussions of kinematic, quasi-kinematic, and dynamic diffraction as well as Lorentz factor effects which are implicit in the experimental diffraction patterns that are shown in this paper.

The {222} reflections are kinematically forbidden for silicon, but are rather strong in all experimental diffraction patterns, Figs. 2b, d, 4, 5, 6b, and c (except in the SAED pattern of the thinnest crystallite, Fig. 6a, where one of these reflections is marked by a full arrow). The special name "perturbation reflections" has been suggested [89] for such reflections and their intensity is partly due to electron diffraction equivalent of the Renninger ("Umweganregungs") effect of X-ray diffraction. The subsequent diffraction of the $(1\bar{1}\bar{3})$ beam on the $(1\bar{1}1)$ net plane results, for example, in the $(2\bar{2}\bar{2})$ reflection.

As also observed by other authors [54], precession electron diffraction at large precession angles and for comparatively thick nanocrystals reduces the intensity of kinematically forbidden reflections significantly. Figures 5b and c show this effect for example for the ±(002) reflections of silicon in the [110] projection. An exponential decay of intensities with precession angle was observed for the kinematically forbidden ±(002) reflections of silicon in the [110] orientation for thicknesses in the range of approximately 22 to 56 nm, Figs. 7 and 8a. Note that the "intensity decay slope" of about one order of magnitude for a precession angle increase of 1° is essentially the same for all silicon crystals throughout this thickness range.

Because the focalization of the precessing primary electron beam onto the sample is not perfect[2], the effective scattering volume of the crystals may also change as a function of the precession angle. Compared to the observed exponential intensity decay of the kinematically forbidden ±(002) reflections of silicon in the [110] projection (within a thickness range of a few tens of nanometers) with increasing precession angle, Figs. 7 and 8a, the peak intensity changes that may be associated with changes in the effective scattering volume are estimated to be negligible.

Figure 8b compares the effect of the precession angle on the intensity of the ±(002), the $\pm(\bar{1}11)$ and $\pm(1\bar{1}1)$ reflections for the 6 nm thin silicon nanocrystal of Fig. 6 with the corresponding dependency of the thickest silicon crystallite of the above mentioned thickness range, Figs. 8a and 5. Principally different dependencies of the (at least partially integrated) intensities of kinematically forbidden and "kinematically allowed" reflections on the precession angle for both crystal thicknesses are revealed in Fig. 8.

While there is essentially the same exponential decay of the intensities for the {002} reflections of the 56 nm thick crystal (as shown in Fig. 7), the kinematically allowed {111} reflection intensities are decreasing much more slowly with precession angle for both low, Fig. 8b, and high, Fig. 8a, crystallite thicknesses and settle to a certain value that is probably determined by thickness dependent primary extinction effects. An apparently exponential decay with a somewhat shallower slope seems to exist for precession angles between about 1.1° and 2.2° for the (002) reflection of the 6 nm thin crystallite, Fig. 8b.

Qualitative similar observations were made for the kinematically forbidden (001) and (003) reflections of an 102 nm thick andalusite (*i.e.* dialuminium silicate oxide,

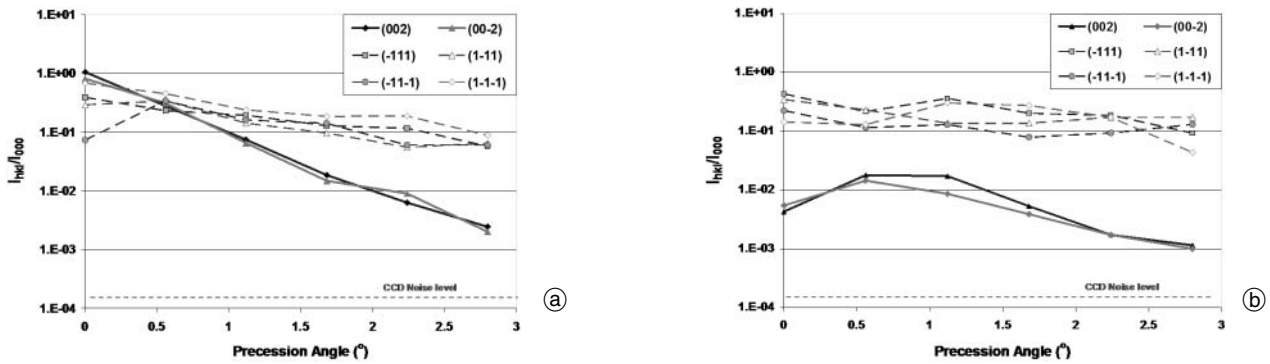

Fig. 8. Effects of the precession angle on the "normalized peak" intensities of the kinematically forbidden ±(002) and the "kinematically allowed" $\pm(\bar{1}11)$ and $\pm(1\bar{1}1)$ reflections that mainly produce them by double diffraction in the [110] zone axis orientation for two silicon crystallites with thicknesses of approximately **(a)** 56 nm and **(b)** 6 nm. The normalization was performed by dividing the maximal peak intensity of the reflections by the maximal peak intensity of the primary electron beam. The relative large difference in the intensities of members of the {111} Friedel pairs in (b) is due to the recording of the diffraction patterns close to the amorphized edge region of the sample, bordering on the vacuum region in the electron microscope, see caption of Fig. 6. (The data were recorded at 200 kV in the nano-beam mode).

$Al_2(SiO_4)O$, with space group Pnnm) crystal in the [110] zone axis orientation [54]. Dynamical multislice simulations for the thickness range of 28 to 126 nm confirmed the near independence of the intensity decay rate of these two kinematically forbidden reflections with increasing precession angle for this mineral [54]. The (002) reflection is in this projection of andalusite the strongest kinematically allowed reflection and its intensity decay with increasing precession angle was qualitatively similar [54] to the behavior of the silicon {111} reflections in Fig. 8.

Note that the strongest kinematically allowed reflections in a ⟨110⟩ projection of silicon are the {111} reflections. A direct comparison of our results to those of Ref. [54] seems, therefore, somewhat justifiable. There must, however, also be significant differences between these two studies since the behavior of kinematically forbidden and allowed reflections with increasing precession angle was in Ref. [54] studied for reflections of a systematic row. Nevertheless, the principally different behavior of kinematically forbidden and allowed reflections with increasing precession angle may allow for a quite unambiguous identification of some of the kinematically forbidden reflections of inorganic crystals and could be utilized for advanced structural fingerprinting in the TEM [6, 7].

The kinematically forbidden ±(002) reflections arise in the [110] projection of silicon mainly from double scattering by the $\pm(\bar{1}11)$ and $\pm(1\bar{1}1)$ reflections. Since four {111} reflections possess the largest net-plane spacing in any ⟨110⟩ projection, the "geometrical part" of the Lorentz factor[6] may enhance their intensities for low nanocrystal thicknesses [56]. This relative intensity increase of the {111} reflections (of any one ⟨110⟩ projection of silicon) should result in more double-diffracted intensity reaching the positions of the two kinematically forbidden {002} reflections (of the respective projection) as well. With increasing precession angle, the effects of the geometric part of the Lorentz factor on the {111} and {002} reflections of a ⟨110⟩ projection of silicon should become weaker. This might be the case for the thinnest nanocrystal of this study, see Figs. 6 and 8b.

While large precession angles reduce secondary scattering effectively, they may also lead to the excitement of reflections from higher order Laue zones (in addition to those from the zero order Laue zone) for certain zone axes of crystals with relative large lattice constants, see Fig. 3e and f. Reflections of higher order Laue zones and of the zero order Laue zone may then superimpose spatially in a large precession angle PED pattern. The respective "superposition diffraction spots" will then possess as intensity the incoherent sum of the intensities of the superimposed reflections from different Laue zones. Such superpositions may, however, be avoided by judicious choices of the precession angle.

The (reciprocal space) radius in a PED pattern below which no overlap of reflections from the zero order Laue zone with their counterparts from a higher order Laue zones is possible[7] may, for this purpose, be estimated by the relation

$$R_{\text{no\_overlap}} = |\vec{k}| \cdot \sin\left(\arccos\left\{\frac{|\vec{k}|\cos\varepsilon - \frac{L_z}{|uvw|}}{|\vec{k}|}\right\} - \varepsilon\right), \tag{10a}$$

[6] The literature so far disagrees about the exact formulae for both parts of the Lorentz factor and under with conditions they must be applied or may be ignored, see, e.g., refs. [34, 41, 56, 57, 69, 70, 72, 74, 77]. The geometric part of the Lorentz factor itself may contain a factor that accounts for the convergence of the primary electron beam (Gjønnes, K.: On the integration of electron diffraction intensities in the Vincent-Midgley precession technique. Ultramicroscopy **69** (1997) 1–11). The thickness dependent part of the Lorentz factor may take a different form for different groups of reflections. One of these forms may be applicably to nearly kinematic reflections, another form to two-beam dynamic reflections, and a third form to reflections in densely packed systematic rows.

For sufficiently thin nanocrystals (that scatter fast electrons nearly kinematically) and a hollow illumination cone without convergence, the Lorentz factor of relation (7) may be approximated to

$$L_{\text{kinematic}} \approx \frac{2}{(ha^* + kb^* + lc^*) \cdot \sqrt{1 - \left(\frac{ha^* + kb^* + lc^*}{R_{\max}}\right)^2}},$$

where a^*, b^* and c^* are the magnitudes of the reciprocal basis vectors, $R_{\max}$ is given by relation (10), and the factor two in the numerator stands for the fact that each reflection is excited (and at least partially integrated) twice during a full 360° cycle of the precessing primary electron beam. For thick crystallites that approximate the asymptotic limit of the Blackman model [30] (and a hollow illumination cone without convergence), relation (7) may to be replaced by

$$\frac{I_{\text{exp}}}{I_0 S} \approx \frac{\frac{\lambda}{\Omega}|F_{hkl}|}{(ha^* + kb^* + lc^*) \cdot \sqrt{1 - \left(\frac{ha^* + kb^* + lc^*}{R_{\max}}\right)^2}},$$

with a Lorentz factor for two-beam dynamical diffraction that is one half of the Lorentz factor for kinematic diffraction.

Note that the latter relation does allow for the extraction of the first power of the structure factor modulus from experimental precession diffraction data [55, 57, 74], whereas the square of the structure factor modulus (times the nanocrystal thickness) can be extracted from kinematical electron precession data [74] according to relation (7). One must be aware, however, that the two-beam approximation neglects double diffraction and dynamical systematic row scattering.

[7] All reflections of the first order Laue zone of silicon in the [110] zone axis orientation are kinematically forbidden by the space group symmetry of $Fd\bar{3}m$. This was the reason for selecting this crystalline material and zone axis for this study! According to relation (11), a PED pattern may for 200 kV electrons and a precession angle of 2.8° extend out to 39 nm^{-1}. With this prediction in mind, the PED simulations for the [110] projection of silicon, Fig. 3d to f, were restricted to 40 nm^{-1}, which is indicated by the outermost ring (of the three concentric rings that are supposed to guide the eye) in these three figures.

Because the atomic scattering factors fall off quickly for electrons with increasing scattering angle, there is typically no measurable intensity for reflections with net-plane spacings of a few tenths of an Ångström. The reflections with the largest reciprocal lattice vectors and appreciable intensity that we observed in the experiments of this study were of the $\{7\bar{7}7\}$ type, *i.e.* at 22.3 nm^{-1}, see Figs. 5c and 6c. All shown reflections of this paper belong to the zero order Laue zone.

For silicon in the [110] orientation, 200 kV electrons, and a precession angle of 2.8°, one obtains from relation (10a) 30.1 nm^{-1} for the "no second-zero order Laue zone overlap radius" of a PED pattern. As Fig. 3f suggests, there should be no reflections form the second order Laue zone in the PED pattern of the study. In comparison for the same experimental parameters, the "no first-zero order Laue zone overlap radius" of a PED pattern is according to relation (10a) just 18.2 nm^{-1}. (Fortunately, as already mentioned above, all of the first order Laue zone reflections are kinematically forbidden for this projection of silicon.)

with $|\vec{k}|$ as magnitude of the electron-wave vector $= \lambda^{-1}$, ε as precession angle, L_z order of the Laue zone, and $|uvw|$ as magnitude of the respective zone axis vector [57]. In a small angle approximation, the sine function in relation (10a) may be replaced by the argument and the no overlap radius with the zero order Laue zone [87] may be obtained in rad by the following relation

$$\varrho_{\text{no\_overlap}} = \arccos\left\{\frac{|\vec{k}|\cos\varepsilon - \frac{L_z}{|uvw|}}{|\vec{k}|}\right\} - \varepsilon\,. \qquad (10b)$$

The maximal (reciprocal space) radial distance of reflections in a PED pattern from the central 000 reflection can be estimated [56] by the relation

$$R_{\max} = 2\,|\vec{k}|\,\sin\varepsilon \qquad (11)$$

where one half of that radial distance is the radius of the Laue circle, see Fig. 3a to c.

Note that relations (10a, b) and (11) were derived for ideal "zero dimensional" reciprocal lattice points (as there is no account of effects of the Fourier transform of the shape function of the crystallite on the diffraction pattern). As a result, both relations will tend to underestimate the respective radii.

Since precession electron diffraction allows for the collection of (at least partially) integrated reflection intensity data, symmetry elements of the crystal are more reliably transferred to the diffraction pattern. As a result of this more reliable transfer of individual symmetry elements, the projected point symmetry[8] becomes a more valuable component of structural fingerprinting in the TEM [6, 7, 83].

When reflections from higher order Laue zones are present in experimental PED patterns[7] (and can be clearly distinguished from their counterparts in the zero order Laue zone), the space group of a nanocrystal may be determined from the point groups of the zero order and higher order Laue zones[8] of a few crystal projections [84–86]. The program "Space Group Determinator" in combination with "CRISP/ELD" from the Calidris company[3] supports such identifications.

A precessing primary electron beam also enhances automated crystal orientations & phases mapping[2] in a TEM significantly [79–81]. The tendencies of PED patterns to show more reflections with kinematic or quasi-kinematic intensity and the suppression of real-structure mediated[5] double-diffraction effects are the causes of this enhancement.

Provided that (at least partially) integrated reflection intensities can be measured with high accuracy and precision and the correct Lorentz factors[6] are used, a suitable modification of the correction scheme from Ref. [35] may be developed on the basis of two (or more) experimental data sets that differ with respect to their "effective curvature" of the Ewald sphere, but are recorded successively from the same crystalline sample area with two (or more) different (*i.e.* smaller and larger) precession angles.

The maximally obtainable precession angle can for any TEM be estimated from the maximally obtainable dark-field tilt angle [61]. For our analytical FEI Tecnai G^2 F20 ST microscope, these maximally obtainable angles are approximately three to four degrees. The spherical aberration coefficient of the objective lens, C_s, sets minimal limits to the electron probe size in precession electron diffraction experiments according to the relation $P_{\min} \approx 4C_s\delta\varepsilon^2$, where δ is the beam-convergence semi-angle, ε the precession angle (in rad), and $d \ll \varepsilon$, Refs. [41, 61]. Precession and de-scanning distortions[2] will increase the obtainable electron probe sizes. The aberrations of the objective lens pre-field will disturb the shape of the probe and may cause it to wander from one sample area to another. These effects will be particularly severe for large precession angles [87, 88].

In order to obtain the smallest electron probe size in a conventional TEM (without an objective lens aberration corrector) the spherical aberration of the objective lens needs to be balanced by the defocus aberration. This is similar to the usual approach for obtaining high resolution phase contrast images [90], but defocus values of several μm rather than tens of nm need to be employed. A side effect of this balancing is the introduction of two-fold astigmatism that depends on both the defocus value and the precession angle. It can be corrected by the objective lens sigmators that all modern microscopes posses. Apart from spherical aberration, the three-fold astigmatism term dominates in conventional TEMs since most instruments are not equipped with a sextupole stigmator [88]. The precessing electron probe may, therefore, take the shape of a "three-lobe star" [87]. For our analytical field-emission TEM with a fixed C_s of 1.2 mm, a 10 μm condenser aperture, and a second generation "Spinning Star"[2], the minimal electron probe size can in the nano-beam mode be adjusted to a few tens of nanometers while utilizing rather large precession angles of up to about 3° degrees.

In state-of-the-art objective lens aberration-corrected TEMs, C_s can be set to arbitrarily low values and balanced

In order to prevent the overlap of reflections from the zero and higher order Laue zones, it has also been proposed to restrict the azimuthal movement of the precessing primary electron beam to a half cycle, *i.e.* 180° degrees, coupled with proper de-scanning [61, 87]. Digital precession electron diffraction add-on instrumentation[2] should be able to do this. One would then obtain on one half of the experimental PED pattern only the reflections from the zero order Laue zone and on the other half only the reflections from the higher order Laue zones in a semi annulus.

[8] Note that the electron diffraction community distinguishes sometimes between "net symmetry", *i.e.* the symmetry of the position of the diffraction spots, and "ideal symmetry" which takes both the position and intensity of the reflections into account [82]. Projected point symmetry (that comprises all 10 groups that exist in 2D for higher order Laue zones) always refers to this ideal symmetry [83]. Due to Friedel's law (applicable for kinematic and quasi-kinematic scattering), only those 6 point symmetry groups that contain a two-fold axis can be distinguished in the zero order Laue zone [9].

The net symmetry is, on the other hand, simply the translation symmetry of the four primitive Bravais lattices that exist in 2D. The 2D centered Bravais lattice is defined by two shortest lattice vectors that possess exactly the same length and intersect with each other at any angle other than 60° or 90° degrees. An example for this are the diffraction patterns from the ⟨110⟩ zone axis of silicon in this paper, where two {111} sports mark the shortest reciprocal lattice vectors that intersect at approximately 70.5°. Orthogonal lattice vectors of unequal length may be chosen as an alternative description, so that the translation symmetry of this lattice is also one of the possible net symmetries.

with fifth order aberrations. Continuously variable precession angles up to about 4° should be obtainable in such microscopes for a stationary probe size of a few nm and without the necessity of re-tuning the shape and apex position of the electron probe when ε is changed in the course of an experiment [87].

Proposal for advanced structural fingerprinting of nanocrystals on the basis of structural data that can be extracted from precession electron diffraction spot patterns

A procedure for structural fingerprinting of nanocrystals on the basis of structural data that can be extracted from precession electron diffraction spot patterns is finally proposed. This procedure possesses three hierarchical levels: extraction and utilization of (i) the projected reciprocal lattice geometry, (ii) the projected point symmetry, and (iii) estimates of the structure factor moduli. As described above, all three levels will benefit from a precessing primary electron beam.

Crystalline materials that have very similar projected reciprocal lattice geometries may well differ in their projected point symmetries and structure factor moduli (even if they have the same element content and a similar stoichiometry). A mixture of nanocrystalline magnetite (Fe_3O_4) and maghemite (γ-Fe_2O_3) can serve here as an example [1]. Individual members of both nanocrystalline phases could be distinguished, *i.e*. fingerprinted structurally in other words, on the basis of high resolution phase contrast transmission electron microscopy images [2–4]. These images needed to be recorded from individual nanocrystals that were in a thickness range were the weak phase object approximation is applicable. Precession electron diffraction should allow for similar distinctions for such iron-oxide nanocrystals that are five to ten times thicker.

Summary and conclusions

This paper outlined the foundations of precession electron diffraction. The utility of this technique for structural fingerprinting of nanocrystals in a transmission electron microscope was alluded to so that this paper complemented our earlier studies. Some of our experimental results with PED on silicon crystals were shown. A brief discussion of powder X-ray fingerprinting and its limitations was also given.

Boris K. Vainshtein and co-workers wrote in 1992: "*For quite a long time the majority of electron diffraction patterns obtained appeared as a store of concealed structural information*", (Ref. [12]). With quite ubiquitous mid-voltage TEMs and the commercial availability of precession electron diffraction add-on instrumentation, the time has come to extract this information and to utilize it not only for structural electron crystallography and the determination of the shape of nanocrystals, but also for advanced structural fingerprinting of nanocrystals on a routine basis.

Acknowledgments. This research was supported by grants from the Office of Naval Research to the Oregon Nanoscience and Microtechnologies Institute. Additional support was provided by Portland State University in the form of Faculty Development, Faculty Enhancement, and Internationalization Awards. Selected members of the International Center for Diffraction Data (and especially members of its Electron Diffraction Subcommittee) are thanked for their encouragement of our developments of novel strategies for structural fingerprinting of nanocrystals. One of the three referees is thanked for suggesting systematic studies of the 2D shape of electron diffraction reflections by precession electron diffraction experiments in order to gain information on the 3D shape of diffracting nanocrystals by comparisons to corresponding simulations on the basis of the kinematic diffraction theory.

References

[1] Moeck, P.; Rouvimov, S.; Nicolopoulos, S.; Oleynikov, P.: Structural fingerprinting of a cubic iron-oxide nanocrystal mixture: A case study. NSTI-Nanotech 2008, Vol. **1**, (2008) 912–915 (www.nsti.org, ISBN 978-1-4200-8503-7); **open access** version of a similar conference paper: arXiv:0804.0063.

[2] Moeck, P.; Bjorge, R.; Mandell, E.; Fraundorf, P.: Lattice-fringe fingerprinting of an iron-oxide nanocrystal supported by an open-access database. Proc. NSTI-Nanotech Vol. **4** (2007) 93–96, (www.nsti.org, ISBN 1-4200637-6-6).

[3] Moeck, P.; Bjorge, R.: Lattice-Fringe Fingerprinting: Structural Identification of Nanocrystals by HRTEM. In: *Quantitative Electron Microscopy for Materials Science* (Eds. E. Snoeck, R. Dunin-Borkowski, J. Verbeeck, U. Dahmen), Mater. Res. Soc. Symp. Proc. Volume **1026E**, Warrendale, PA, 2008, **on line** as paper 1026-C17-10; http://www.mrs.org/s_mrs/sec_subscribe.asp?CID=11354&DID=208171&action=detail.

[4] Bjorge, R.: Lattice-Fringe Fingerprinting: Structural Identification of Nanocrystals Employing High-Resolution Transmission Electron Microscopy. *Master of Science thesis*, Portland State University, May 9, 2007; published on the Internet after peer review in Journal of Dissertation, Vol. **1**, Issue 1, 2007; **open access**: http://www.scientificjournals.org/journals2007/j_of_dissertation.htm.

[5] Moeck, P.; Fraundorf, P.: Structural fingerprinting in the transmission electron microscope: Overview and opportunities to implement enhanced strategies for nanocrystal identification. Z. Kristallogr. **222** (2007) 634–645.

[6] Moeck, P.; Rouvimov, S.: Structural fingerprinting of nanocrystals in the transmission electron microscope: utilizing information on projected reciprocal lattice geometry, 2D symmetry, and structure factors. In: *Drug Delivery Nanoparticles Formulation and Characterization* (Eds. Y. Pathak, D. Thassu), Informa, 2009 (Drugs and the Pharmaceutical Sciences, Vol. **191**), pp. 270–313, (ISBN-13: 978-1-4200-7804-6).

[7] Moeck, P.; Rouvimov, S.; Nicolopoulos, S.: Precession electron diffraction and its utility for structural fingerprinting in the transmission electron microscope, Proc. 2009 NSTI Nanotechnology Conference and Trade Show, Vol. **I**, 417–420 (www.nsti.org, ISBN: 978-1-4398-1782-7).

[8] Moeck, P.: Database supported nanocrystal structure identification by lattice-fringe fingerprinting with structure factor extraction. United States Patent 20080275655, published: November 6, 2008, priority date: May 3, 2007; **open access:** http://www.freepatentsonline.com/20080275655.pdf.

[9] Vainshtein, B. K.: Structure Analysis by Electron Diffraction. Pergamon Press Ltd., Oxford, 1964.

[10] Vainshtein, B. K.: Modern Crystallography in Four Volumes, Vol. **I**, Symmetry of Crystals, Methods of Structural Crystallography. Springer Series in Solid-State Sciences **15**, Springer, Berlin Heidelberg, New York, 1981.

[11] Vainshtein, B. K.: Diffraction Investigation of the Atomic Structure of Matter: The Ewald lecture delivered on 26 July 1990 at the XV Congress of the International Union of Crystallography, Bordeaux, France. Acta Cryst. B**47** (1991) 145–154.

[12] Vainshtein, B. K.; Zvyagin, B. B.; Avilov, A. S.: Electron Diffraction Structure Analysis, In: *Electron Diffraction Techniques* (Ed. J. M. Cowley), Vol. **1**, pp. 216–312, Oxford University Press, Oxford 1992.

[13] Vainshtein, B. K.; Zvyagin, B. B.: Electron-diffraction structure analysis. In: *International Tables for Crystallography*, Vol. **B**, Reciprocal space, (Ed. U. Shmueli), 2nd edition, Kluver Academic Publ., Dordrecht, 2001, pp. 306–320.
[14] Pinsker, Z. G.: II.15. Development of Electron Diffraction Structure Analysis in the USSR, In: *Fifty Years of Electron Diffraction* (Ed. P. Goodman), Reidel Publish. Comp., Dordrech, Boson, London, 1981, pp. 155–163.
[15] Zou, X. D.; Hovmöller, S.: Electron crystallography: imaging and single-crystal diffraction from powders. Acta Cryst. A **64** (2008) 149–160; **open access:** http://journals.iucr.org/a/issues/2008/01/00/issconts.html.
[16] http://nanocrystallography.research.pdx.edu/CIF-searchable/cod.php and http://nanocrystallography.research.pdx.edu/search.py/index.
[17] Gražulis, S.; Chateigner, D.; Downs, R. T.; Yokochi, A. F. T.; Quirós, M.; Lutterotti, L.; Manakova, E.; Butkus, J.; Moeck, P.; Le Bail, A.: Crystallography Open Database an open access collection of crystal structures. J. Appl. Cryst. **42** (2009) 726–729; **open access:** http://journals.iucr.org/j/issues/2009/04/00/kk5039/kk5039.pdf.
[18] http://cod.ibt.lt/ (in Lithuania) *mirrored at* http://www.crystallography.net, http://cod.ensicaen.fr/ (both in France) *and* http://nanocrystallography.org, http://nanocrystallography.net (both in Oregon, USA, *the latter mirror is currently the only one that allows for three-dimensional interactive displays of all entries of the COD at the atomic level*).
[19] http://nanocrystallography.research.pdx.edu.
[20] Fraundorf, P.; Qin, W.; Moeck, P.; Mandell, E.: Making sense of nanocrystal lattice fringes. J. Appl. Phys. **98** (2005) 114308; **open access:** arXiv:cond-mat/0212281 v2; Virtual Journal of Nanoscale Science and Technology Vol. **12** (2005) Issue 25.
[21] Moeck, P.; Čertik, O.; Upreti, G.; Seipel, B.; Harvey, M.; Garrick, W.; Fraundorf, P.: Crystal structure visualizations in three dimensions with support from the open access Nano-Crystallography Database. J. Materials Education **28** (2006) 83–90.
[22] Faber, J.; Blanton, J.: Full pattern comparison of experimental and calculated powder patterns using the Integral Index method in PDF-4+. Powder Diffraction **23** (2008) 141–149.
[23] Hanawalt, J. D.; Rinn, H. W.: Identification of crystalline materials: Classification and use of X-ray diffraction patterns. Ind. Eng. Chem. Anal. Ed. **8** (1936) 244–247.
[24] Faber, J.; Fawcett, T.: The Powder Diffraction File: present and future. Acta Cryst. B **58** (2002) 325–332.
[25] Ungár, T.: Microstructure of nanocrystalline materials studied by powder diffraction. Z. Kristallogr. Suppl. **23** (2006) 313–318.
[26] Pinna, N.: X-Ray diffraction from nanocrystals. Progr. Colloid. Polym. Sci. **130** (2005) 29–32.
[27] Kaszkur, Z.: Test of applicability of some powder diffraction tools to nanocrystals. Z. Kristallogr. Suppl. **23** (2006) 147–154.
[28] Pielaszek, R.; Łojkowski, W.; Matysiak, H.; Wejrzanowski, T.; Opalinska, A.; Fedyk, R.; Burjan, A.; Proykova, A.; Iliev, H.: In: *8th Nanoforum Report: Nanometrology* (Eds. W. Lojkowski, R. Turan, A. Proykova, A. Daniszewska), pp. 79–80, July 2006, **open access:** www.nanoforum.org.
[29] Petkov, V.; Zavalij, P. Y.; Lutta, S.; Whittingham, M. S.; Parvanov, V.; Shastri, S.: Structure beyond Bragg: Study of V_2O_5 nanotubes. Phys. Rev. B **69** (2004) 85410.
[30] Blackman, M.: On the intensities of electron diffraction rings. Proc. Royal Society (London) A **173** (1939) 68–82.
[31] Cowley, J. M.: Crystal Structure Determination by Electron Diffraction. Progress in Materials Science, Vol. **13**, 267–321, (Eds. B. Chalmers, W. Hume-Rothery), Pergamon Press, Oxford, 1967.
[32] Gjønnes, J.: The Dynamic Potentials in Electron Diffraction. Acta Cryst. **15** (1962) 703–707.
[33] Klechkovskaya, V. V.; Imamov, R. M.: Electron Diffraction Structure Analysis – from Vainshtein to Our Days. Crystallography Reports **46** (2001) 534–549.
[34] Gjønnes, K.; Cheng, Y.; Berg, B. S.; Hansen, V.: Corrections for Multiple Scattering in Integrated Electron Diffraction Intensities; Application to Determination of Structure Factors in the [001] Projection of Al_mFe. Acta Cryst. A **54** (1998) 102–119.
[35] Dorset, D. L.: Structural Electron Crystallography. Plenum Press, New York and London, 1995.
[36] Komrska, J.: Algebraic expressions of shape amplitudes of polygons and polyhedra. Optik **80** (1987) 171–183.
[37] Neumann, W.; Komrska, J.; Hofmeister, H.; Heydenreich J.: Interpretation of the Shape of Electron Diffraction Spots from Small Polyhedral Crystals by Means of the Crystal Shape Amplitude. Acta Cryst. A **44** (1988) 890–897.
[38] J. Komrska, J.; Neumann, W.: Crystal Shape Amplitudes of Platonic Polyhedra I. General Aspects and the Shape Amplitudes of the Tetrahedron, Cube, and Octahedron. phys. stat. sol. (a) **150** (1995) 89–111.
[39] Neumann, W.; Komrska, J.: Crystal Shape Amplitudes of Platonic Polyhedra II. The Regular Pentagonal Dodecahedron and the Icosahedron. phys. stat. sol. (a) **150** (1995) 113–126.
[40] Xiong, Y.; Wiley, B. J.; Xia, Y.: Nanocrystals with unconventional shapes – A class of promising catalysts. Angew. Chem. Int. Ed. **46** (2007) 7157–7159.
[41] Vincent, R.; Midgley, P.: Double conical beam-rocking system for measurement of integrated electron diffraction intensities. Ultramicroscopy **53** (1994) 271–282.
[42] Buerger, M. J.: The precession method in X-ray crystallography. John Wiley and Sons, Inc. New York, London, Sydney, 1964.
[43] Hoppe, W.: Three-Dimensional Low Dose Reconstruction of Periodical Aggregates. In: *Unconventional Electron Microscopy for Molecular Structure Determination* (Eds. W. Hoppe, R. Mason), Friedrich Vieweg & Sohn, Braunschweig, Wiesbaden, 1979, pp. 191–220; (Advances in Structure Research by Diffraction, Vol. **7**).
[44] Krakow, W.; Howland, A.: A method for producing hollow cone illumination electronically in the conventional transmission electron microscope. Ultramicroscopy **2** (1976) 53–67.
[45] Mugnaioli, E.; Gorelik, T.; Kolb, U.: "Ab initio" structure solution form electron diffraction data obtained by a combination of automated diffraction tomography and precession technique. Ultramicroscopy **109** (2009) 758–765.
[46] Kolb, U.; Gorelik, T.; Mugnaioli, E.: Automated diffraction tomography combined with electron precession: a new tool for *ab initio* nanostructure analysis. In: *Electron Crystallography for Materials Research and Quantitative Characterization of Nanostructured Materials* (Eds. P. Moeck, S. Hovmöller, S. Nicolopoulos, S. Rouvimov, V. Petkov, M. Gateshki, P. Fraundorf), Mater. Res. Soc. Symp. Proc. Volume **1184**, pp. 11–24, Warrendale, PA, 2009, ISBN: 978-1-60511-157-5, **on line** as paper 1184-GG01–05; http://www.mrs.org/s_mrs/sec_subscribe.asp?CID=18405&DID=243543&action=detail.
[47] Klein, H.; Gemmi, M.; Rageau, A.: Solving Unknown Complex Oxide Structures by Precession Electron Diffraction: Ag-CoO_2, $PbMnO_{2.75}$ and $LiTi_{1.5}Ni_{0.5}O_4$. In: *Electron Crystallography for Materials Research and Quantitative Characterization of Nanostructured Materials* (Eds. P. Moeck, S. Hovmöller, S. Nicolopoulos, S. Rouvimov, V. Petkov, M. Gateshki, P. Fraundorf), Mater. Res. Soc. Symp. Proc. Volume **1184**, pp. 25–36, Warrendale, PA, 2009, ISBN: 978-1-60511-157-5, **on line** as paper 1184-GG01–06; http://www.mrs.org/s_mrs/sec_subscribe.asp?CID=18405&DID=242716&action=detail.
[48] Georgieva, D.: Electron Crystallography of Three Dimensional Protein Crystals, PhD thesis, University of Leiden, December 12, 2008.
[49] Dudka, A. P.; Avilov, A. S.; Lepeshov, G. G.: Crystal structure refinement from electron diffraction data. Crystallography Reports **53** (2008) 530–536.
[50] Gilmore, C. J.; Dong, W.; Dorset, D. L.: Solving the crystal structures of zeolites using electron diffraction data. I. The use of potential-density histograms. Acta Cryst. A **64** (2008) 284–294.
[51] Gilmore, C. J.; Dong, W.; Dorset, D. L.: Solving the crystal structures of zeolites using electron diffraction data. II. Density-building functions. Acta Cryst. A **64** (2008) 295–302.
[52] Xie, D.; Baerlocher, C.; McCusker, L. B.: Combing precession electron diffraction data with X-ray powder diffraction data to facilitate structure solution. J. Appl. Cryst. **41** (2008) 1115–1121.
[53] Boulahya, K.; Parras, M.; González-Calbet, J. M.; Nicolopoulos, S.: Ab initio structure determination of heavy oxide $Sr_9Mn_5Co_2O_{21}$ from precession electron diffraction data. Phys. Chem. News **41** (2008) 15–19.

[54] Ciston, J.; Deng, B.; Marks, L. D.; Own, C. S.; Sinkler, W.: A quantitative analysis of the cone-angle dependence in precession electron diffraction. Ultramicroscopy **108** (2008) 514–522.
[55] Sinkler, W.; Own, C. S.; Marks, L.: Application of a 2-beam model for improving the structure factors from precession electron diffraction intensities. Ultramicroscopy **107** (2007) 543–550.
[56] Oleynikov, P.; Hovmöller, S.; Zou, X. D.: Precession electron diffraction: Observed and calculated intensities. Ultramicroscopy **107** (2007) 523–533.
[57] Gemmi, M.; Nicolopoulos, S.: Structure solutions with three-dimensional sets of precessed electron diffraction intensities. Ultramicroscopy **107** (2007) 483–494.
[58] Dudka, A. P.; Avilov, A. S.; Nicolopoulos, S.: Crystal structure refinement using Bloch-wave method for precession electron diffraction. Ultramicroscopy **107** (2007) 474–482.
[59] Dorset, L. D.; Gilmore, C. J.; Jorda, J. L.; Nicolopoulos, S.: Direct electron crystallographic determination of zeolites zonal structures. Ultramicroscopy **107** (2007) 462–473.
[60] Boulahya, K.; Ruiz-González, L.; Parras, M.; González-Calbet, J. M.; Nickolsky, M. S.; Nicolopoulos, S.: Ab initio determination of heavy oxide perovskite related structures from precession electron diffraction data. Ultramicroscopy **107** (2007) 445–452.
[61] Avilov, A.; Kuligin, K.; Nicolopoulos, S.; Nickolskiy, M.; Boulahya, K.; Portillo, J.; Lepeshov, G.; Sobolev, B.; Collette, J. P.; Martin, N.; Robins, A. C.; Fischione, P.: Precession technique and electron diffractometry as new tools for crystal structure analysis and chemical bonding determination. Ultramicroscopy **107** (2007) 431–444.
[62] Klein, H.: Electron crystallography applied to a "real" sample: the structure of Mn_2O_3 solved by precession electron diffraction, Colloque SFì-2007, Grenoble, June 5–8, 2007; **open access:** http://sfmu2007.free.fr/files/resumespdf/Klein_sfmu2007.pdf.
[63] Kverneland, A.; Hansen, V.; Vincent, R.; Gjønnes, K., Gjønnes, J.: Structure analysis of embedded nano-sized particles by precession electron diffraction. η'-precipitate in an Al–Zn–Mg alloy as example. Ultramicroscopy **106** (2006) 492–502.
[64] Weirich, T. E.; Portillo, J.; Cox, G.; Hibst, H.; Nicolopoulos, S.: Ab initio determination of the framework structure of the heavy-metal oxide $Cs_xNb_{2.54}W_{2.46}O_{14}$ from 100 kV precession electron diffraction data. Ultramicroscopy **106** (2006) 164–175.
[65] Dorset, D. L.; Weston, S. C.; Dhingra, S. S.: Crystal Structure of Zeolite MCM-68: A New Three-Dimensional Framework with Large Pores. J. Phys. Chem. B **110** (2006) 2045–2050.
[66] Dorset, D. L.: The crystal structure of ZSM-10, a powder X-ray and electron diffraction study. Z. Kristallogr. **221** (2006) 260–265.
[67] Own, C. S.; Marks, L. D.; Sinkler, W.: Precession electron diffraction 1: multislice simulation. Acta Cryst. A **62** (2006) 434–443.
[68] Own, C. S.; Sinkler, W.; Marks, L. D.: Rapid structure determination of a metal oxide from pseudo-kinematical electron diffraction data. Ultramicroscopy **106** (2006) 114–122.
[69] Own, C. S.: System Design and Verification of the Precession Electron Diffraction Technique. PhD thesis, Northwestern University, 2005; **open access**: http://www.numis.northwestern.edu/Research/Current/precession.shtml.
[70] Own, C. S.; Subramanian, A. K.; Marks, L. D.: Quantitative Analyses of Precession Diffraction Data for a Large Cell Oxide. Microsc. Microanal. **10** (2004) 96–104.
[71] Gjønnes, J.; Hansen, V.; Kverneland, A.: The Precession Technique in Electron Diffraction and its Application to Structure Determination of Nano-Size Precipitates in Alloys. Microsc. Microanal. **10** (2004) 16–20.
[72] Gemmi, M.; Zou, X. D.; Hovmöller, S.; Migliori, M.; Vennström, M.; Andersson, Y.: Structure of Ti_2P solved by three dimensional electron diffraction data collected with precession technique and high resolution electron microscopy. Acta Cryst. A **59** (2003) 117-126.
[73] Gjønnes, J.; Hansen, V.; Andersen, S. J.; Marioara, C. D.; Li, X. Z.: Electron crystallography of aluminum alloy phases. Z. Kristallogr. **218** (2003) 293–307.
[74] Gemmi, M.; Calestani, G.; Migliori, A.: Strategies in Electron Diffraction Data Collection. In: *Advances in Imaging and Electron Physics*, Vol. **123**, Microscopy, Spectroscopy, Holography and Crystallography with Electrons (2002) 311–325, Academic Press, (Eds. P. W. Hawkes, P. G. Merli, G. Calestani, M. Vittori-Antisari).
[75] Gemmi, M.: Precession technique, In: *Electron Crystallography and Cryo-Electron Microscopy on Inorganic Materials and Organic and Biological Molecules* (Eds. J. Puiggali, A. Rodriquez-Galan, L. Franco, M. Casas), Universitat Politecnica De Catalunya, Barcelona, 2001, p. L91–L97.
[76] Gjønnes, J.; Hansen, V.; Berg, B. S.; Runde, P.; Cheng, Y. F.; Gjønnes, K.; Dorset, D. L.; Gilmore, C. J.: Structure model for the phase Al_mFe derived from three-dimensional electron diffraction intensity data collected by a precession technique. Comparison with convergent-beam diffraction. Acta Cryst. A **54** (1998) 306–319.
[77] Berg, B. S.; Hansen, V.; Midgley, P. A.; Gjønnes, J.: Measurement of three-dimensional intensity data in electron diffraction by the precession technique. Ultramicroscopy **74** (1998) 147–157.
[78] Midgley, P. A.; Sleight, M. E.; Saunders, M.; Vincent, R.: Measurement of Debye-Waller factors by electron precession. Ultramicroscopy **75** (1998) 61–67.
[79] Rauch, E. F.; Véron, M.; Portillo, J.; Bultreys, D.; Maniette, Y.; Nicolopoulos, S.: Automatic Crystal Orientation and Phase Mapping in TEM by Precession Diffraction. Microscopy and Analysis, Issue 93, November 2008, S5–S8.
[80] Rouvimov, S.; Rauch, E. F.; Moeck, P.; Nicolopoulos S.: Automated Crystal Orientation and Phase Mapping of Iron Oxide Nano-Crystals in a Transmission Electron Microscope, Proc. 2009 NSTI Nanotechnology Conference and Trade Show, Vol. **I**, 421–424 (www.nsti.org, ISBN: 978-1-4398-1782-7).
[81] Moeck, P.; Rouvimov, S.; Rauch E. F.; Nicolopoulos, S.: Structural Fingerprinting of Nanocrystals: Advantages of Precession Electron Diffraction, Automated Crystallite Orientation and Phase Maps. In: *Electron Crystallography for Materials Research and Quantitative Characterization of Nanostructured Materials* (Eds. P. Moeck, S. Hovmöller, S. Nicolopoulos, S. Rouvimov, V. Petkov, M. Gateshki, P. Fraundorf), Mater. Res. Soc. Symp. Proc. Volume **1184**, Warrendale, PA, 2009, pp. 49–60, ISBN: 978-1-60511-157-5, **on line** as paper 1184-GG03–07; http://www.mrs.org/s_mrs/sec_subscribe.asp?CID=18405&DID=242718&action=detail.
[82] Jacob, D.; Cordier, P.; Morniroli, J.-P.; Schertl, H.-P.: Application of precession electron diffraction to the characterization of (021) twinning in pseudo-hexagonal coesite. American Mineralogist **94** (2009) 684–692.
[83] Moeck, P.; Rouvimov, S.: Two-dimensional symmetry determinations for structural fingerprinting in the transmission electron microscope. Proc. 2009 NSTI Nanotechnology Conference and Trade Show, Vol. **I**, 323–326 (www.nsti.org, ISBN: 978-1-4398-1782-7).
[84] Morniroli, J. P.; Ji, G.: Identification of the kinematical forbidden reflections from precession electron diffraction. In: *Electron Crystallography for Materials Research and Quantitative Characterization of Nanostructured Materials* (Eds. P. Moeck, S. Hovmöller, S. Nicolopoulos, S. Rouvimov, V. Petkov, M. Gateshki, P. Fraundorf), Mater. Res. Soc. Symp. Proc. Volume **1184**, Warrendale, PA, 2009, pp. 37–48, ISBN: 978-1-60511-157-5, **on line** as paper 1184-GG01–03; http://www.mrs.org/s_mrs/sec_subscribe.asp?CID=18405&DID=246640&action=detail.
[85] Morniroli, J. P.; Redjaïmia, A.; Nicolopoulos, S.: Contribution of electron precession to the identification of the space group from microdiffraction patterns. Ultramicroscopy **107** (2007) 514–522.
[86] Morniroli, J. P.; Redjaïmia, A.: Electron precession microdiffraction as a useful tool for the identification of the space group. J. Microsc. **227** (2007) 157–171.
[87] Own, C. S.; Sinkler, W.; Marks, L. D.: Prospects for aberration corrected electron precession. Ultramicroscopy **107** (2007) 534–542.
[88] Own, C. S.; Dellby, N.; Krivanek, O. L.; Marks, L. D.; Murfitt, M.: Aberration-corrected precession electron diffraction. Microsc. Microanal. **13**, Suppl. 2, (2007) 96–97.
[89] Heidenreich, R. D.: Theory of the "Forbidden" (222) Electron Reflection in the Diamond Structure. Phys. Rev. **77** (1950) 271–283.
[90] Spence, J. C. H.: High-Resolution Electron Microscopy, 3rd edition. Oxford University Press, Oxford 2003 (Monographs on the Physics and Chemistry of Materials 60).